



Cite this: *Soft Matter*, 2018,  
14, 6756

## Formation of three-dimensional colloidal crystals in a nematic liquid crystal

Yiwei Wang, <sup>a</sup> Pingwen Zhang<sup>\*a</sup> and Jeff Z. Y. Chen <sup>\*bc</sup>

We investigate the possible structures of three-dimensional colloidal crystals formed when these spherical particles are dispersed in a liquid crystal. The case of a strong homeotropic boundary condition is considered here. Their corresponding defect structures in the space-filler nematic liquid crystal are induced by the presence of the spherical surface of the colloids and produce an attraction between colloidal particles. Here, a standard Landau-de Gennes free energy model for a spatially inhomogeneous liquid crystal is numerically minimized to yield an optimal configuration of both spherical colloids and the orientational field. The stable and metastable structures obtained in this work are described and analyzed according to the type of periodic liquid-crystal defect lines that couple the colloidal spheres together. A large range of the spherical size is covered in this study, corresponding to a 5CB-liquid-crystal comparison for assembling micron- to nano-sized colloidal spheres. Multiple configurations are found for each given particle size and the most stable state is determined by a comparison of the free energies. From large to small colloidal particles, a sequence of structures, which range from quasi-one-dimensional (columnar), to quasi-two-dimensional (planar), and to truly three-dimensional, are found to exist.

Received 22nd May 2018,  
Accepted 22nd July 2018

DOI: 10.1039/c8sm01057a

rsc.li/soft-matter-journal

### 1 Introduction

A colloidal crystal is a spatially ordered array of colloidal particles. Building novel colloidal structures, including colloidal crystals, is one of the most active areas in modern colloidal science. Liquid-crystal colloids, which are dispersions of discrete colloidal particles in a liquid crystal containing anisotropic orientational ordering itself, have been proven to be a new and efficient tool to achieve this goal. The presence of colloidal particles disrupts the orientational ordering of liquid crystals locally and generates topological defects near the particle surface; in turn these defects couple colloidal particles together to form colloidal crystals.<sup>1</sup>

During the last decades, a large amount of work has been devoted to studying colloidal structures formed in liquid crystals.<sup>2–11</sup> It has been shown that multiple colloidal particles in a nematic liquid crystal can self-assemble to form one-dimensional (1D) linear chains<sup>2,7</sup> or two-dimensional (2D) colloidal crystals.<sup>3–6,9–11</sup> The experimental realization of three-dimensional (3D) colloidal crystals in a nematic is relatively rare; Nych *et al.*, for example, recently produced a 3D nematic colloidal crystal, known as the dipolar crystal, experimentally.<sup>12</sup> Normally, at nano to micron

length scales, isotropically shaped colloidal particles are modeled by solid spheres. They are attracted to each other due to indirect interactions, induced by the much smaller liquid-crystal molecules that act as a space filler between colloidal spheres. The orientational properties of these liquid-crystal molecules are usually modeled by an orientational field which is treated as a continuous function of spatial coordinates.

One common way to understand the physical mechanisms for building higher-level structures is to extend the ideas we have already learnt from lower-level structures, such as the compound structures of liquid crystals with one or two colloidal particle(s) in the bulk.<sup>2,4,5,7,13</sup> The anchoring of liquid crystal molecules on the surface of colloidal spheres highly influences the continuous nematic orientational field and due to geometry frustration, produces orientational field defects, anisotropically placed around the colloidal sphere(s). For example, under the right conditions, a single sphere can produce a small defect ring in the nematic liquid above the north pole. Effectively, this can be viewed as a single dipole configuration in comparison with electrostatics.<sup>14</sup> Just as multiple dipole molecules can form a head-to-tail 1D configuration, the physical mechanism of forming a 1D colloidal chain can be understood as assembly of effective colloidal dipoles, heads to tails.<sup>2,4</sup>

The uniqueness of liquid-crystal-colloid compounds is the mutual influence of the colloidal configuration and surrounding nematic field which cannot be separated. Take the example of the 1D dipolar linear configuration. As multiple 1D dipolar chains

<sup>a</sup> LMAM and School of Mathematical Sciences, Peking University, Beijing, 100871, P. R. China. E-mail: pzhong@pku.edu.cn

<sup>b</sup> Department of Physics and Astronomy, University of Waterloo, Waterloo, Ontario, N2L 3G1, Canada. E-mail: jeffchen@uwaterloo.ca

<sup>c</sup> School of Chemistry, Beihang University, Beijing 100191, P. R. China

are placed near each other, the space-filling nematic field seeks further reduction of the overall free energy by adjusting its orientational field; this could simply yield a weak binding attraction between chains, hence the resulting 3D configuration is identifiable as a quasi-1D structure, or this could generate a complete rewiring of the defect lines to enable a more closely coupled structure. The defect pattern is dependent on the relative position of the adjacent colloidal spheres. Hence, to theoretically determine the structure of a liquid-crystal colloidal crystal, a model free energy (such as Landau-de Gennes used here) for the spacing-filling liquid crystal must be minimized simultaneously with respect to both the orientational field and relative colloidal positioning.

Recently, Čopar *et al.* took an interesting approach in which a 3D opal-like, closely packed face-centered-cubic (fcc) crystal structure is assumed. They then ask the question of how many topologically different ways can defect lines be wired in the building voids where the liquid crystal fills. Once this answer emerges, one can then use them as the elementary building blocks to classify the defect network.<sup>15</sup> Experimentally, such an opal-like system was also studied by Kang *et al.*, in which a different way to decompose the defect networks was proposed.<sup>16</sup> We understand from ref. 15 that in the systems they studied, the solid spheres are in contact with each other to form a rigid structure; this could be regarded as a porous medium filled with a nematic liquid crystal.<sup>17–19</sup>

We take a different approach here by deforming the elementary computation cells from the ideal conditions. In this work, we start by taking a primitive, body-centered, base-centered, or face-centered unit cell and assume the space-filling liquid crystal can be described by the LdG free energy as a function of a tensor orientational order parameter  $Q(\mathbf{r})$  [see Section 2 and Appendix A]. Both  $Q(\mathbf{r})$  and the unit cell parameters (including the cell lengths and cell angles) are allowed to vary in a minimization procedure [see Appendices]. The LdG theory contains two system parameters,  $\tau$  and  $1/\xi_R$ , for which  $\tau$  can be identified with a customarily used value in liquid crystal 5CB.<sup>1,4–8,20,21</sup> The other parameter,  $1/\xi_R$ , can be related to the reduced colloidal particle radius and is used as an adjustable system parameter here [see Appendix B]. In order to employ the spectral representation of the order parameter tensor in a deformable unit cell [see Appendix C], we use a numerical trick to properly set up the homeotropic boundary conditions at the surfaces of the spherical colloidal particles [see Appendix D]. The free energy is then minimized with respect to both  $Q(\mathbf{r})$  and unit-cell parameters such as cell lengths and cell angles. The procedure gives rise to a liquid-crystal-colloid configuration, corresponding to a free-energy minimum, locally or globally, with a deformable crystal structure.

The obtained structures are analyzed in Section 3, where we pay attention to how defect lines couple the colloidal particles together. The structures are classified as quasi-1D, quasi-2D, and true 3D in subsections, according the coupling of colloidal spheres to their neighbors. As a unit cell is not uniquely defined for a given periodic structure, the same defect-colloid structure can be calculated and viewed in different types of unit cells.

Whenever possible, we also present a face-centered perspective based on the positions of the almost closely packed colloidal spheres. Beyond a few highly symmetric structures, most structures found here have a face-centered unit cell where the lengths and angles are not idealized.

The free-energy branches of these structures as functions of  $1/\xi_R$  allow us to determine the most stable structures that have the lowest free energies, as described in Section 4. While most of the determined structures fit into the topological categories defined in ref. 15, we discover new types of liquid crystal defects in the colloid-crystal voids, complementary to those already discussed. The result, of course, is prediction of new crystalline structures beyond those in ref. 15.

## 2 Model

To study the current system we adopt a conventional approach and assume that the free energy contains two parts. The first is the LdG free energy  $F$ , which is a functional of the order-parameter tensor  $Q(\mathbf{r})$  used to describe the local orientational ordering of the background liquid crystal. In its reduced version,

$$F = \left\{ \frac{\tau}{2} \text{tr}(Q^2) - \frac{\sqrt{6}}{4} \text{tr}(Q^3) + \frac{1}{4} [\text{tr}(Q^2)]^2 + \frac{\xi_R^2}{2} |\nabla Q|^2 \right\} d\mathbf{r}, \quad (1)$$

where  $\mathbf{r}$  describes the spatial coordinates written in units of  $R$ ,  $\tau$  is a dimensionless temperature-like parameter, and  $\xi_R$  is a dimensionless ratio between the bending rigidity of the nematic texture and the radius of the spherical colloidal particles. The one-elastic-constant approximation is made here.<sup>1,4–8,20,21</sup>

The second is the surface anchoring energy to model the interaction between the immersed spherical colloidal particles and the liquid crystal. We impose a surface energy that enforces strong homeotropic anchoring at the spherical surfaces,

$$F_s = \frac{w}{2} \int |Q(\mathbf{r}) - Q_s(\mathbf{r})|^2 dA, \quad (2)$$

where the integration is carried out over all surfaces  $A$  of colloidal particles and  $Q_s$  is fixed at  $S_0(3\mathbf{n}_s \otimes \mathbf{n}_s - I)/2$  with  $S_0 = \sqrt{2}(3 + \sqrt{9 - 64\tau})/(8\sqrt{3})$ . The anchoring strength  $w$  is chosen to be significantly large to model the strong homeotropic anchoring condition.<sup>22–30</sup>

In order to numerically find the structures of three-dimensional colloidal crystals, we focus on a single unit cell lattice and assume periodic solutions at all lattice boundaries. The order parameter  $Q(\mathbf{r})$  is expanded in terms of a standard Fourier series in which the main- $\mathbf{k}$  vectors are considered up to the truncated term. The coefficients of the Fourier bases are determined by a standard optimization method such as the Limited-memory Broyden-Fletcher-Goldfarb-Shanno (L-BFGS) algorithm,<sup>31</sup> which adjusts all coefficients during optimization. The strong homeotropic anchoring at the surface of colloidal particles is dealt with by the fictitious domain method.<sup>32</sup> A unit lattice used in the computation can contain  $n$  ( $n = 1, 2, 3, 4$ ) colloidal spheres by considering a primitive, body-centered, base-centered, or face-centered unit cell. Subsequently, the periodicity of the unit lattice and the cell angles

are adjusted during optimization by a derivative-free optimization method such as the Mesh Adaptive Direct Search (MADS).<sup>33</sup> The details of the numerical method can be found in the Appendices.

We draw isosurfaces of the orientational order parameter  $S(\mathbf{r})$ , which is the largest eigenvalue of  $Q$ ,<sup>1</sup> or isosurfaces of the Westin metric  $c_l$ , which is the difference between the two largest eigenvalues of  $Q$ ,<sup>34</sup> to visualize the topological defects. The resulting effect is a thick, connected curve.

### 3 Results: stable and metastable structures

The numerical results presented below are for a fixed  $\tau = -0.2234^{1,4-8,20,21}$  and an adjustable particle size through varying  $1/\xi_R$ . The minimization of the free energy with respect to  $Q(\mathbf{r})$  in a 3D space produces a stable solution [*i.e.*, corresponding to a (hopefully) global minimum] or a metastable solution (*i.e.*, a local minimum) for a given set  $[\tau, \xi_R]$ . The stability of each structure is assessed by examination of the reduced free-energy per particle

$$f_n = \frac{F_n - F_b}{n\xi_R^2}, \quad (3)$$

where  $F_n$  is the lattice free-energy minimum and  $F_b$  is the free energy of the undistorted liquid crystal in the unit cell.

Among the fifteen 3D structures found in this work, the six illustrated in Fig. 1 have dominating low free-energies in the corresponding parameter regions shown in Fig. 1(g). Many of these defect structures are manifested from the defect

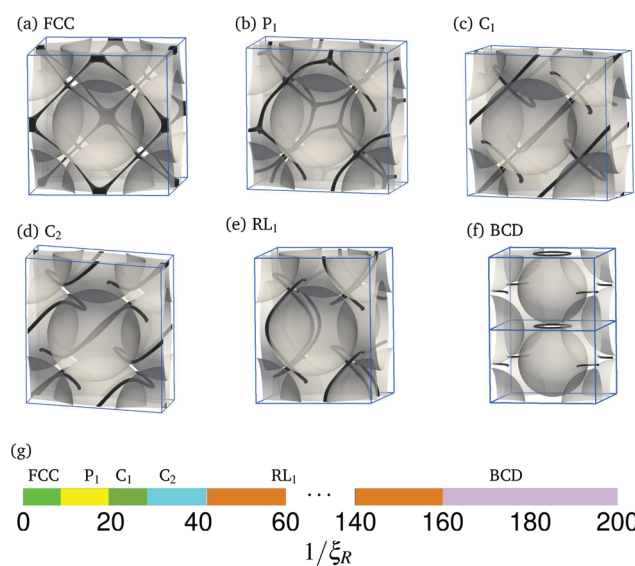


**Fig. 1** Three-dimensional stable structures of colloidal crystals formed in a nematic liquid crystal, found in this work by numerically minimizing the LdG free energy at room temperature according to the 5CB parameterizations. The optimized unit cells of P<sub>1</sub>, C<sub>1</sub> and C<sub>2</sub> are not right rectangular prisms. The structures are plotted at  $\xi_R = 0.1768$  [(a) for FCC], 0.08839 [(b) for P<sub>1</sub>], 0.03536 [(c) for C<sub>1</sub>], 0.03536 [(d) for C<sub>2</sub>], 0.03536 [(e) for RL<sub>1</sub>], and 0.007071 [(f) for BCD]. The domain of the particle size,  $1/\xi_R$ , is divided into a 1D phase diagram for the free-energy-preferred colloid-defect structures in (g).

structures known as the dipolar and quadrupolar states, when a single spherical particle is placed in a bulk liquid crystal.<sup>2,4,14,23</sup> Some of the structures can be traced back to formation of colloidal dimers found recently<sup>2,7,20</sup> and some are unique in their 3D arrangement. We dissect these structures, together with other metastable structures, below.

#### 3.1 Quasi-1D structure: BCD

The simplest 3D structure is the body-centered dipolar crystal (BCD), which is found here to be stable when  $1/\xi_R \gtrsim 160$  (corresponding to  $R \gtrsim 1.2 \mu\text{m}$  in 5CB). The quasi-1D structure can be clearly traced back to the dipole configuration found from the system of a single colloidal sphere placed in a large liquid crystal cell, which is energetically preferred when  $1/\xi_R \gtrsim 220$  in its own environment.<sup>13</sup> The 3D structure turns out to have a larger stability domain.

In comparison with electrostatics, the compound of the single colloidal sphere and associated defect ring in the liquid crystal could be regarded as an electric dipole moment, pointing vertically in Fig. 2(a). It is now well known that two of these structures can form a stable dipolar pair, pointing head to tail.<sup>35</sup> A 1D dipolar colloidal chain, all in the head-to-tail formation, can be experimentally made in a real liquid crystal containing multiple dipolar compounds.<sup>2,4</sup>

The 3D structure in Fig. 2 could be viewed as further stacking of these chains to form a right-angle columnar structure with a square base; the closest neighboring chains are shifted in the  $z$ -direction by half of the center-to-center distance within a column. Theoretically, Chernyshuk *et al.* demonstrated that the octopole moment plays an important role in the formation of such a 3D nematic colloidal crystal in the framework of Oseen-Frank theory.<sup>36</sup> The blue unit cell of BCD shown in Fig. 2 is a body-centered rectangular prism with equal unit-cell lengths on the base and a shorter unit-cell length vertically. The values of these cell dimensions were adjusted in our computation to achieve the free-energy minimum. In the final equilibrium structure, we obtained  $a = b \approx 3.08R$  and  $c \approx 2.09R$  for  $\xi_R = 0.007071$  ( $R \approx 1 \mu\text{m}$  in 5CB), which is in agreement with the values measured experimentally in ref. 12 [ $a = b = (3.2 \pm 0.1)R$ ,  $c = (2.3 \pm 0.2)R$ ]; furthermore, they also agree with the values predicted theoretically in ref. 36 ( $a = b = 3.07R$ ,  $c = 2.44R$ ). Experimentally, in a recent publication, Nych *et al.* reported that

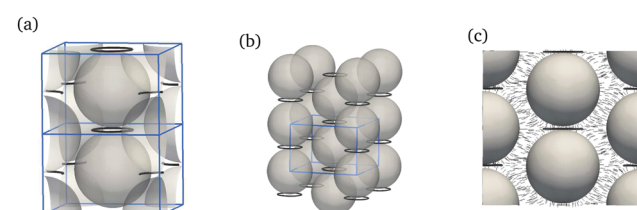


**Fig. 2** Different perspectives of BCD at  $\xi_R = 0.007071$ . Plot (a) shows the colloid-defect structure in two body-centered unit cells. Plot (b) illustrates how stacking of 1D dipolar colloidal chains forms a 3D structure. The cross-section structure in the (110) plane is shown in (c) together with the main nematic director. The black rings, representing the liquid crystal defects, are drawn by iso-surfaces of  $S = 0.5$ .

BCD can be stabilized when 4  $\mu\text{m}$  colloidal particles self-assemble themselves in a bulk liquid crystal (ZLI-2806).<sup>12</sup>

### 3.2 Quasi-1D structure: columnar

Previously, a number of groups reported that the defect patterns around a pair of intruding spherical colloids can re-arrange significantly to display entangled or unentangled defect lines. In the case of multiple colloidal spheres, the rearrangement of defects can be viewed as rewiring the defect lines to cover multiple spheres. Among them, a class of quasi-1D, columnar (C) structures appear metastable and stable, as shown in Fig. 3(a). These 3D structures can be viewed as stacking of two basic types of 1D colloidal chains, represented by columns (unfilled and grey), alternately arranged in the  $x$ - $y$  plane. The colloidal particles in unfilled columns are shifted along the vertical direction from those in grey columns by about half of the sphere–sphere distance along a chain.

The compositions of the two columns in the first two states,  $C_1$  and  $C_2$ , are identical. In comparison with the defect patterns of colloidal-dimer formation,  $C_1$  and  $C_2$  can be related to the so-called entangled-hyperbolic-defect (H) and unentangled-defect (U) dimer pairs, respectively.<sup>7,20,24</sup> Instead of the one-to-one coupling of a dimer pair, the same defect pattern links

all spheres along the 1D direction. This was observed in previous experimental and numerical studies.<sup>7,20</sup> The 3D stacking pattern follows the illustration in Fig. 3(a).

The two columns in  $C_3$ ,  $C_4$ ,  $C_5$ , and  $C_6$  are made of different types of defect structures.  $C_3$  contains “H coupling” and “U coupling”, as a natural mixing of typical columns in  $C_1$  and  $C_2$ .  $C_4$  contains H coupling along the grey columns and the so-called figure-of-Omega defect (O) which entangles two (and only two) nearest spheres along the unfilled columns.  $C_5$  contains O coupling along the grey columns and the so-called figure-of-eight defect (E) which entangles two (and only two) nearest spheres along the unfilled columns.  $C_6$  is similar to  $C_4$ , where the grey columns are made of H-coupled spheres. The O-coupled spheres in the unfilled columns now involve all spheres. The 3D stacking pattern follows the illustration in Fig. 3(b).

Going back to the basic symmetries of these states, we note that these are all right-angled columnar, *i.e.*, the column-axis is at a right angle with respect to the column base. A two-fold rotational symmetry about the column-axis exists in  $C_1$ ,  $C_2$  and  $C_3$ . The same rotation brings  $C_4$  (also  $C_5$  and  $C_6$ ) to a different state  $C_4'$  (also  $C_5'$  and  $C_6'$ ) that has a degenerate free-energy to the original. The symmetry of all states can be viewed in an alternative perspective. Cutting through all nearest-neighboring spheres in all grey columns and using this plane as the new  $x$ - $y$  plane, we can show that the structure can be represented in a face-centered parallelepiped unit cell, with the old  $z$  axis sitting along the direction that connects two adjacent, face-centered spheres. The illustration in Fig. 3(c) is for  $C_4$ , which has three types of colloidal spheres in different symmetry environments. All edge lengths of this new perspective are different.

This section describes the types of 3D defect states, which are relatively stable and relatively easy to find, appearing in our calculations. One could imagine, for example, a state that contains O in one column and U in another, or H in one column and E in another. Many combinations could exist along this direction of thought. Note that one column in  $C_4$  or  $C_5$  is made of a sequence of entangled sphere-doublets. Structurally, to make it more complicated, one could also imagine that a single column contains a sequence of sphere-triplets or other types of multiplets, or even a sequence that contains a mixing of different types of multiplets. To build beyond the scenario of two column types, the 3D system could even include three (or more) types of columns—the combination is almost endless. This would require that the computation box is extended to a much larger cell. So far, we have restricted ourselves to a basic face-centered calculation box and found that these columnar structures can be stabilized when  $1/\xi_R \gtrsim 20$  (corresponding to  $R \gtrsim 150 \text{ nm}$  in 5CB).

### 3.3 Quasi-2D structures: planar structures

A number of quasi-2D structures can be stabilized in the system. Typically, three identical layers of planar crystals stack on top of each other, shifted along the 2D plane from each other, as shown in Fig. 4(a). Each layer contains 2D defect structures in the liquid crystal that couple the colloidal particles closely in a plane.

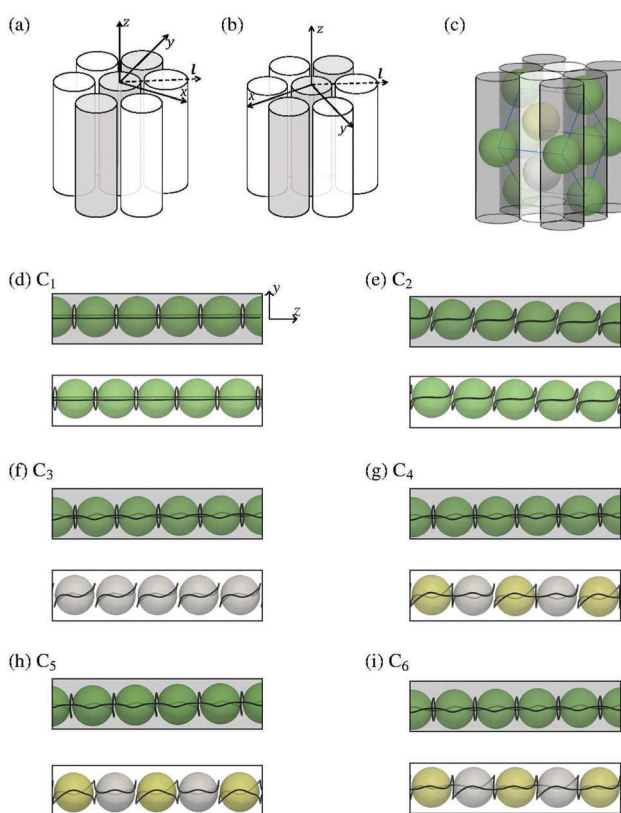


**Fig. 3** Columnar structures for  $\xi_R = 0.03536$ . Plots (a and b) illustrate two types of column arrangement for columns with grey and unfilled shades. Taking a different perspective, these columnar structures could be viewed to have a face-centered parallelepiped unit cell as in plot (c). The two types of columns are shown in (d–i) for  $C_1$ ,  $C_2$ , ... and  $C_6$ , respectively. Spheres that have the same symmetry environment carry the same color.

Among these, the hexagonal planar  $P_1$  is energetically preferred in the small  $1/\xi_R$  range. The colloidal spheres self-organize in a perfect 2D hexagonal lattice, caged by connected defect lines around every particle, which themselves form a 2D hexagonal defect lattice as well. As can be seen in Fig. 4(c) the structure maintains a six-fold rotation about the  $z$ -axis. There is no direct defect line coupling between layers and as such the spacing between the two nearest layers is larger than the sphere–sphere distance of the 2D hexagonal packing. Within the range  $11 \lesssim 1/\xi_R \lesssim 20$  (corresponding to  $80 \text{ nm} \lesssim R \lesssim 150 \text{ nm}$  in 5CB),  $P_1$  has the lowest free energy among those studied in this paper, and hence is considered stable, shown by the phase diagram in Fig. 1.

Two other planar, metastable structures can be stabilized relatively easily, to yield local free energy minima in a larger  $1/\xi_R$  domain, as illustrated in Fig. 4(d) and (e).  $P_2$  contains two types of identifiable defect-line patterns in a layered plane. From the top-view of the 2D plane, a large, S-shaped loop couples multiple spheres together. Smaller ring-shaped defect loops can also be found in the liquid crystal between adjacent spheres. In each layer,  $P_3$  is built from a repeated, 2D pattern that involves

four colloidal spheres as a braid. They form a parallelogram shown by four colors in Fig. 4(e). Both large defect loops in  $P_2$  and  $P_3$  are different from those seen in systems consisting of a bulk liquid crystal and isolated single or double colloidal particles. Although the 2D lattice structures of  $P_2$  and  $P_3$  resemble an almost hexagonal lattice, a careful examination reveals that the 6-fold rotational symmetry about the vertical axis is replaced by a 2-fold rotational symmetry.

An fcc-like view is shown in Fig. 4(b), where the coupled layers are also explicitly labeled as cross-sections. The face-centered unit cell of  $P_1$  is a rhombohedron with non-right angles and equal cell lengths ( $a = b = c \approx 2.99R$ ,  $\alpha = \beta = \gamma \approx 88.4^\circ$ ). In contrast, the face-centered unit cells of  $P_2$  and  $P_3$  are both parallelepipeds with non-right angles and unequal cell lengths.

The formation of 2D crystals by packing colloidal particles either in a thin nematic film<sup>9</sup> or at a nematic–air interface<sup>37</sup> was reported previously. For example, Ravnik and Žumer *et al.* constrained their study of the same LdG model on a rectangular, body centered 2D unit cell with a periodic boundary condition. Along the perpendicular direction from the 2D plane, the liquid crystal was assumed to extend in a 3D box of a size 4-times the colloidal radius; the boundary conditions of the background liquid crystal at the top and bottom of the box are assumed to be in the same “rubbing” direction. We take a different approach here. We obtained all structures directly from a 3D parallelepiped unit cell with periodic boundary conditions in all three directions. The final analysis of the resulting 3D defect structures then leads to our conclusion that these three structures can be considered stacking of layers.

### 3.4 Quasi-2D structure: RL

There exists another type of quasi-2D structures. Within a 2D layer the defect lines glue colloidal particles into a 2D crystal where a rectangular unit cell can be identified. The 3D rectangularly layered (RL) structures are periodic stacking of these 2D rectangles vertically, as schematically shown in Fig. 5(a).

The first is  $RL_1$ , for which the 2D layers can be viewed in Fig. 5(d). A basic, single-sphere defect pattern is accompanied by a strongly bent defect ring that stretches across a large region. The ring configuration itself more resembles a dipolar configuration in a single-sphere case, but two ends of the defect ring are stretched to near-equator positions. Two typical layers can be viewed in the figure, with the colloid-defect-ring direction reversed in alternative layers. Due to the built-in symmetry of the layered structure, the final 3D unit cell is a face-centered right rectangular prism with unequal sides, as schematically shown in Fig. 5(b).

For comparison, layers in  $RL_2$  contain more closely coupled 2D structures, as shown in Fig. 5(e). Both layers have exactly the same pattern but one shifts in the figure’s diagonal direction by half the diagonal sphere–sphere distance. A typical, stretched defect ring now intercalates among four colloidal spheres together. Due to the interwound pattern, each layer has a square symmetry. As a consequence, the unit cell in the final stacked 3D structure is a body-centered right square prism, or equivalently, a larger face-centered right square prism, as shown in Fig. 5(c).

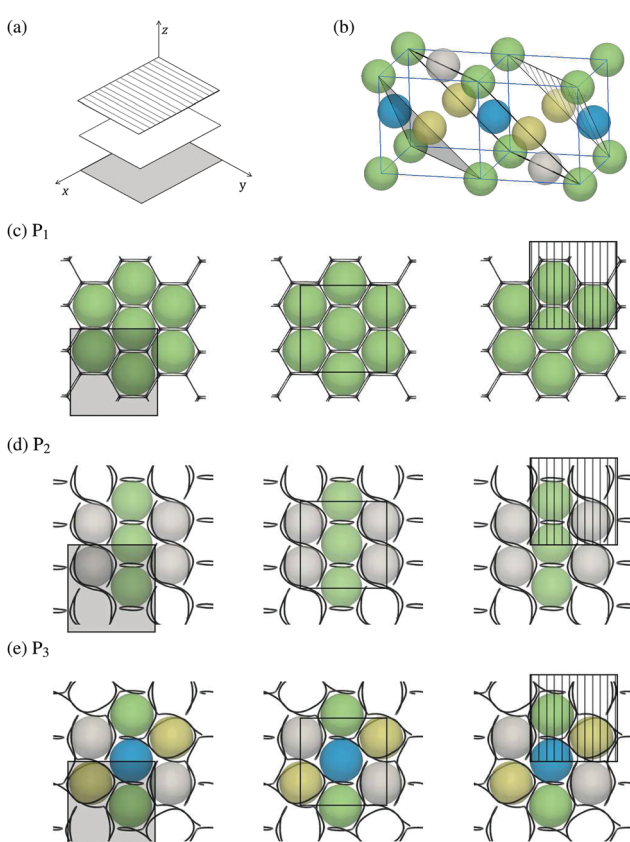


**Fig. 4** Planar structures which contain three different layers of closely coupled colloids. The three layers are represented by grey-filled, unfilled, and line-shaded patterns, as indicated in (a). Three planar structures are found here, at  $\xi_R =$  (c) 0.08839, (d) 0.03536, and (e) 0.03536. The layer types are labeled in (c), (d) and (e). Colloidal spheres having the same symmetry environments are represented by the same color. Plot (b) takes an imperfect face-centered view of  $P_3$  across two unit cells. For illustration purposes, the radii of spheres shown in plot (b) are reduced to half of their actual sizes.

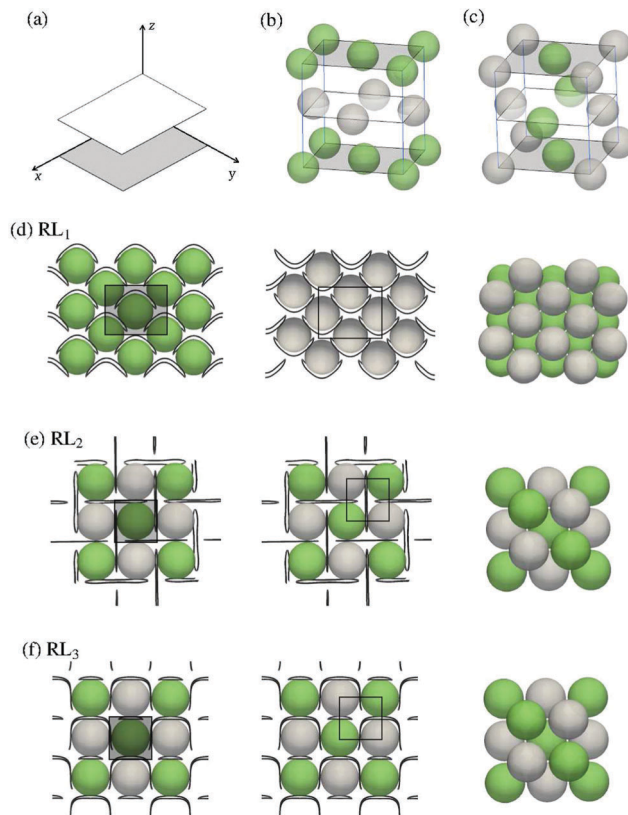


**Fig. 5** Rectangularly layered structures found in this work. Plot (a) shows that there are basically two identical types of layers in each structure, grey-filled and unfilled. The calculations were actually performed in a face-centered unit cell, shown in (b and c), where the unit-cell angles and side lengths are unconstrained. Plots (d–f) display the two types of layered structure (left and middle panels) and the 3D stacked structure (right panel). These particular examples were all produced at  $\xi_R = 0.03536$  for RL<sub>1</sub>, RL<sub>2</sub>, and RL<sub>3</sub>. For illustration, the radii of spheres shown in plots (b and c) are reduced to half of their actual sizes.

RL<sub>3</sub> is also a layered structure with an identical pattern shown in each layered  $x$ - $y$  plane [see Fig. 5(f)]. Two typical defect rings can be identified. The first is an extensively deformed defect ring that glues four spheres together in a triangle formation. A single defect ring, resembling the defect ring in a dipolar ring of a single particle configuration, appears between two spheres and further connects the lattice together in a network. Layer by layer, the 3D structure is built, in a similar way as in RL<sub>2</sub>. The structure, however, has a two-fold rotational symmetry about  $z$ , not four-fold. Because of its particular symmetry, the final body-centered unit cell of RL<sub>3</sub> is a right rectangular prism with unequal sides, and the final face-centered unit cell in RL<sub>3</sub> is a right prism with a diamond-shaped base.

Among these three structures, RL<sub>1</sub> has the lowest free energy for large- $1/\xi_R$ , as discussed in Section 4.1. The formation of these rectangular layered structures is a consequence of bending and stretching of defect rings, which can be viewed as new ways of arranging unentangled rings—these arrangements become possible with multiple spheres.

### 3.5 3D defect structures

From our computations, true 3D structures that contain 3D defect structures, which couple the colloidal particles in a 3D crystal formation, can be stabilized in a small particle range,  $1/\xi_R \lesssim 11$ . Taking the 5CB liquid crystal as an example, we estimate that these structures exist when the sizes of the colloidal particles are in the nanometer range ( $R \lesssim 80$  nm).

The most stable (*i.e.*, low free-energy) 3D structure, FCC, has colloidal particles placed in a perfect face-centered cubic unit cell. An fcc unit cell is illustrated in Fig. 1(a), where each colloidal sphere is caged inside a regular, connected network of defect lines. The structures can be viewed in a smaller, body-centered tetragonal unit cell, as illustrated in Fig. 6(a), where the rhombic-dodecahedron-like cage can be seen clearly. The defect structure in FCC is closely related to the entangled-hyperbolic-defect (H) structure in the dimer problem.<sup>7,24</sup> Instead of forming a defect ring between two closest particles like H, a parallelogram-shaped loop, which is a facet of the rhombic-dodecahedron, appears here.

Approximately within the same  $1/\xi_R$  range, another highly symmetric 3D structure, BCC, can be stabilized, but has a higher minimized free energy than that of FCC. As illustrated in Fig. 6(b), the colloidal spheres are placed in a perfect body-centered cubic lattice. Around each colloidal sphere, the defect lines form a truncated-octahedron-like cage. Although BCC is metastable (*i.e.* has a higher free-energy minimum than that of FCC as shown in the inset of Fig. 7(a)), it is quite stable against small perturbations in the optimal  $Q$  profile and the optimal unit cell obtained by our numerical solution. That is, BCC is trapped in a free-energy minimum which means that it could be observed experimentally to coexist with FCC.

## 4 Discussion

### 4.1 Comparison between free energies

All the structures illustrated in the last section are obtained from minimizing the LdG model, each within its own range of  $1/\xi_R$ . Globally, for a given  $1/\xi_R$  these free energy minima are compared and the lowest is deemed stable. Fig. 1(g) shows the one-dimensional phase diagram, as the result of this comparison.

Fig. 7 displays all free-energy branches (per colloidal particle) where the symbols represent the results from the actual numerical

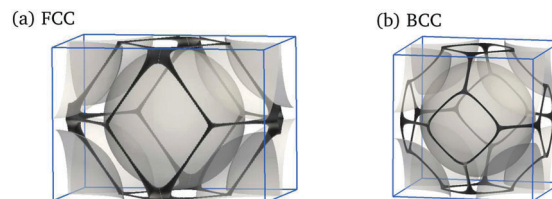


**Fig. 6** 3D structures found in this work: (a) FCC (face-centered cubic) and (b) BCC (body-centered cubic). In plot (a), FCC is shown in a body-centered unit cell, in which  $a = 3.06R$ , and  $b = c = 2.16R$  ( $1/\xi_R = 0.1768$ ). Plot (b) is produced for  $\xi_R = 0.1768$ , which has the reduced unit cell length  $a = b = c = 2.46R$ .

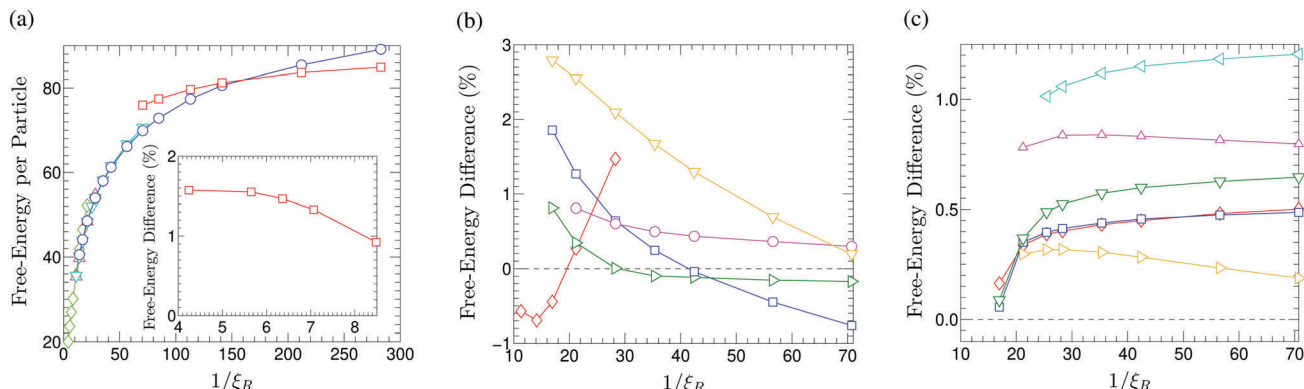


**Fig. 7** Free-energy minima calculated for all structures studied in this work, as functions of the particle size  $1/\xi_R$ . Plot (a) shows the reduced free energies over the entire  $1/\xi_R$  range for FCC [diamonds],  $P_1$  [up-triangles],  $C_1$  [down-triangles],  $RL_1$  [circles], and BCD [squares]. The inset shows the free energy difference of BCC with the free energy of FCC as the reference, as a function of  $1/\xi_R$ . In an expanded view, plot (b) shows the reduced free-energy differences of  $P_1$  [diamonds],  $C_2$  [right-triangles],  $RL_1$  [squares],  $RL_2$  [circles], and  $RL_3$  [down-triangles], with the free energy of  $C_1$  [dash-line] as the reference. Similarly, plot (c) shows the reduced free energy difference of  $C_3$  [diamonds],  $C_4$  [squares],  $C_5$  [left-triangles],  $C_6$  [up-triangles],  $P_2$  [right-triangles], and  $P_3$  [down-triangles], with the free energy of  $C_1$  [dash-line] as the reference.

solutions to the LdG model. The curves behind the symbols are the interpolations from these data points for different structures. The phase boundary in Fig. 1(g) is determined from the crossing points of these curves in Fig. 7(a) and (b). To clearly display features of the free energy, in plots (b) and (c) relative free-energy differences are shown with the free energy of  $C_1$  as the reference.

All transitions between the defect states listed in Fig. 1 are considered first-order phase transitions, as all the free energy branches in Fig. 7 cross each other. Because of the different ways of wiring the defect lines in these structures, physically, going through a phase transition from one state to another requires rewiring of the defect lines; hence the phase transition is of a discontinuous nature.

A few general trends can be deduced from the sequence of stable defect states determined in this work. The first feature is that from high  $1/\xi_R$  to low  $1/\xi_R$ , the stable states settle from less ordered structures (mostly quasi-1D and quasi-2D) to more ordered structures (FCC). This is accompanied by the transition from loose packing to close packing of the colloidal particles. We can compare the phase diagram in Fig. 1(g) for the periodic

colloidal crystals with the phase diagrams obtained for the single- and dimer-colloid problems.<sup>13</sup> In the high  $1/\xi_R$  region, the stability region of BCD in Fig. 1(g) is similar in size to that of the dipole preferred region in the single particle problem.

#### 4.2 Symmetries of the 3D crystals

The 3D colloidal crystals presented above, together with the defect structures in the liquid crystals, are dissected according to specific symmetries. Whenever possible, we also present these structures in face-centered parallelepiped unit cells. Table 1 shows the optimal parameters of face-centered parallelepiped unit cells of these structures obtained from our computation. Among these, only  $RL_1$  and  $RL_2$  are right rectangular prisms and FCC is a perfectly face-centered cube, due to the built-in symmetries.

The analysis by Čopar *et al.* for defect networks was performed in a closely packed face-centered cubic cell.<sup>15</sup> They predicted a variety of possible structures, followed by a general argument of wiring defect lines in the liquid-crystal spacing between the periodic colloidal particles. Regardless of the fact that some of our

**Table 1** Optimal parameters of the structures discussed in this paper. All colloidal particles are placed in a view with a face-centered parallelepiped unit cell that has three unit-cell vectors: **a**, **b** and **c**. The angles  $\alpha$ ,  $\beta$ , and  $\gamma$  are those between  $(\mathbf{a}, \mathbf{b})$ ,  $(\mathbf{a}, \mathbf{c})$ , and  $(\mathbf{b}, \mathbf{c})$ , respectively

Structure	$\xi_R$	Optimal parameters					
		$a/R$	$b/R$	$c/R$	$\alpha$	$\beta$	$\gamma$
$C_1$	0.03536	$2.95 \pm 0.05$	$2.95 \pm 0.05$	$3.18 \pm 0.05$	$(87.8 \pm 0.5)^\circ$	$(89.4 \pm 0.5)^\circ$	$(88.6 \pm 0.5)^\circ$
$C_2$	0.03536	$2.92 \pm 0.05$	$3.08 \pm 0.05$	$3.13 \pm 0.05$	$(88.6 \pm 0.5)^\circ$	$(87.7 \pm 0.5)^\circ$	$(88.7 \pm 0.5)^\circ$
$C_3$	0.03536	$2.90 \pm 0.05$	$3.06 \pm 0.05$	$3.11 \pm 0.05$	$(87.9 \pm 0.5)^\circ$	$(87.8 \pm 0.5)^\circ$	$(88.5 \pm 0.4)^\circ$
$C_4$	0.03536	$2.96 \pm 0.05$	$2.95 \pm 0.05$	$3.10 \pm 0.05$	$(87.8 \pm 0.5)^\circ$	$(89.4 \pm 0.5)^\circ$	$(88.6 \pm 0.5)^\circ$
$C_5$	0.03536	$2.95 \pm 0.05$	$2.95 \pm 0.05$	$3.07 \pm 0.05$	$(87.8 \pm 0.5)^\circ$	$(89.4 \pm 0.5)^\circ$	$(88.6 \pm 0.5)^\circ$
$C_6$	0.03536	$2.95 \pm 0.05$	$2.95 \pm 0.05$	$3.13 \pm 0.05$	$(87.8 \pm 0.5)^\circ$	$(89.4 \pm 0.5)^\circ$	$(88.7 \pm 0.5)^\circ$
$P_1$	0.08839	$2.99 \pm 0.05$	$a$	$a$	$(88.4 \pm 0.5)^\circ$	$\alpha$	$\alpha$
$P_2$	0.03536	$3.08 \pm 0.05$	$3.08 \pm 0.05$	$2.90 \pm 0.05$	$(88.7 \pm 0.5)^\circ$	$(88.5 \pm 0.5)^\circ$	$(88.4 \pm 0.5)^\circ$
$P_3$	0.03536	$2.93 \pm 0.05$	$3.04 \pm 0.05$	$3.09 \pm 0.05$	$(87.8 \pm 0.5)^\circ$	$(88.2 \pm 0.5)^\circ$	$(88.3 \pm 0.5)^\circ$
$RL_1$	0.03536	$2.52 \pm 0.05$	$3.23 \pm 0.05$	$3.40 \pm 0.05$	$90^\circ$	$90^\circ$	$90^\circ$
$RL_2$	0.03536	$2.95 \pm 0.05$	$a$	$3.15 \pm 0.05$	$90^\circ$	$90^\circ$	$90^\circ$
$RL_3$	0.03536	$2.95 \pm 0.05$	$a$	$3.13 \pm 0.05$	$(89.5 \pm 0.5)^\circ$	$90^\circ$	$90^\circ$
FCC	0.1768	$3.06 \pm 0.05$	$a$	$a$	$90^\circ$	$90^\circ$	$90^\circ$

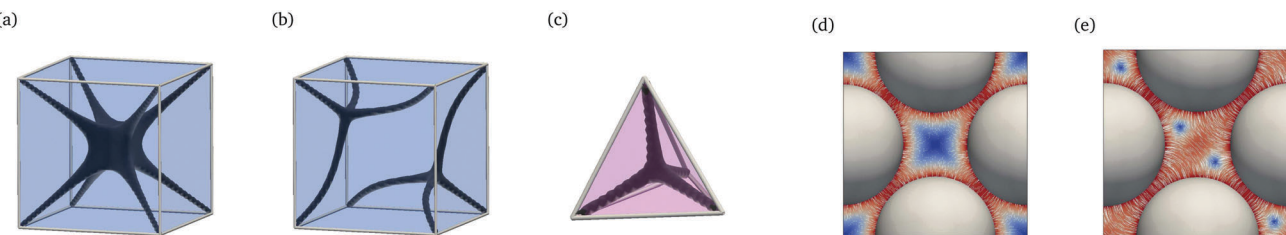


**Fig. 8** New elementary building blocks of the liquid crystal fillers induced by colloidal spheres in an fcc unit cell, beyond those described in ref. 15. Structures (a–c) contains defect lines that show up in FCC,  $P_1$  and  $C_1$  (small- $1/\xi_R$ ). The cross-section views of the nematic directors are displayed for further comparison: in (d) the middle cross section of FCC for  $\xi_R = 0.1768$  and in (e) the middle cross section of  $P_1$  for  $\xi_R = 0.08839$ . The colors in (d and e) are arranged according to the largest eigenvalue of  $Q$  such that high to low values correspond to color variation from red to blue.

findings destroy the perfect conditions (angles and side lengths) of an fcc lattice, in an fcc-like view, most of defect-colloid structures found here can be categorized by the type of defect spacings described by these authors [see their Fig. 1]. Of course, the arrangements of colloidal particles are highly influenced by the symmetries of the spacing defect lines. We demonstrated in the above that there is no intrinsic reason for most of these structures to form a perfect fcc unit cell.

Using Čopar *et al.*'s description in an fcc-like unit cell, we find that the defect lines in the liquid-crystal spacings of our FCC,  $P_1$  and  $C_1$  (small- $1/\xi_R$ ) are of new types. For example, the cubic void that borders the six spherical particles in FCC has the defect structure shown in Fig. 8(a), where the central region is a connected defect. In a more revealing illustration, the liquid crystal defect can be seen at the center of Fig. 8(d), which illustrates the cross-section view of the nematic directors by cutting the fcc cell in the middle through the face-centered colloidal spheres. The tetrahedron void defined in ref. 15 now has a four branched defect structure connected at the center [Fig. 8(c)].

Another new defect pattern is the cube-like voids in  $P_1$ , as illustrated in Fig. 8(b), where two defect centers connect the four-branched defect lines. Again, cutting through the unit cell in the middle we illustrate a typical nematic director pattern in Fig. 8(e). The defect structure in tetrahedron voids in  $P_1$  is the same as the one illustrated in Fig. 8(c).

To summarize, our calculations have demonstrated that new building blocks (*i.e.*, the defect structures in the liquid crystal voids that border the colloidal particles) exist, beyond those described in ref. 15. They have the characteristics of connecting multiple branches of defect lines together by a central defect region. Some of the most stable states found here are built from these basic units in the small- $1/\xi_R$  range.

## 5 Summary

In this work, we numerically solved the LdG model to find the free-energy minima and their corresponding optimal structures of liquid-crystal-colloidal-particle crystals, in a three-dimensional space. The stable and metastable structures are described and analyzed according to the type of liquid crystal defect lines that couple the colloidal spheres together. A large range of the particle

size is covered in this study, corresponding to a 5CB comparison for assembling micron- to nano-sized colloidal spheres. From large to small colloidal particles, we observe a sequence of structures that are quasi-one-dimensional (columnar), quasi-two-dimensional (planar), or true three-dimensional. The most stable state for a given particle size is determined by a comparison of the free energies and illustrated in a phase diagram. Some of the free-energy branches, though, have small differences, which indicate that the metastable defect states can be well-populated in real systems. The study is carried out by using the one-distortion-coefficient approximation. An alternative approximation may change the theoretical stabilities of these states.

Most of the computations in the current work are carried out in a unit cell that has a parallelepiped shape. The procedure allows us to determine the optimal structures generally without *a priori* assumption of the resulting symmetry. The unit cell's edge lengths and the deformation angles are all subject to free-energy minimization. Though most of the structures found here have the face-centered cubic symmetry approximately, we clearly specified the symmetries of each structure in a simple language of how defect lines in the liquid crystal are used to glue the colloidal spheres together.

The current study, as well as the study in ref. 15 (which was performed in a closely packed fcc unit cell), assumes a single face-centered unit cell with period boundary conditions as the starting point. This assumption, however, can only handle structures with a "short" defect-line periodicity. We observe, for example, the formations of two-particle braids in  $C_4$  and  $C_5$ , and a four-particle braid in  $P_3$ , as the basic building blocks. We have not extended our basic unit cell to contain two (or more) face-centered cells. These extended cells would allow us to discover states where the defect lines (hence the colloids) have an extended length of a basic unit. The question of whether these possible new structures exist remains a question for future study.

Beyond the periodic crystal structures, experimentally, many other 2D colloidal clusters formed by micron-sized dipolar and quadrupolar colloidal particles have been observed.<sup>6,8,38,39</sup> For example, by using laser tweezers, Ognista *et al.* assembled a large variety of 2D clusters. More recently, complex 2D colloidal assemblies with low packing densities, including polygon-rings, squares, and tetrahedra were built by placing micron-sized dipolar particles together.<sup>40,41</sup> Although these complex structures

are difficult to form through self-assembly, they can be energetically more stable than the simple formation of a finite-sized linear chain. A theoretical understanding based on free energy analysis, along this direction of structural formation, is still missing, either for 2D<sup>6,8,38,39</sup> or 3D<sup>12</sup> clusters.

The formation of colloidal crystals due to their associated liquid crystal defects can often be compared with the formation of atomic crystals with valence bonds.<sup>42</sup> Indeed, using this comparison properly, we can build a higher order structure by binding these “atoms” to form a colloidal crystal. This comparison, however, is incomplete. Defects in the immersed liquid crystals are produced by the presence of spheres themselves and multiple colloidal spheres can produce different environments. The mutual influences make the “atoms” multi-colored: they can change the types of entangle defect structures around themselves and introduce new ways of gluing the colloidal particles together. The large variety of defect patterns in the liquid crystal voids seen here, as well as those discussed in ref. 15, demonstrates this point.

The model used here is based on the so-called one-elastic constant approximation, suitable for describing a nematic background liquid crystal. Recent studies showed that 3D colloidal crystals can be stabilized in a cholesteric liquid crystal<sup>30</sup> and a blue-phase liquid crystal;<sup>43</sup> these systems are beyond the scope of the current study.

## Conflicts of interest

There are no conflicts to declare.

## Appendix

### A The reduced version of LdG theory

The full expression for the LdG model contains an expansion of the free energy in  $Q$  up to  $\mathcal{O}(Q^4)$  and in the spatial derivatives of  $Q$  up to the quadratic terms,<sup>44,45</sup>

$$F[Q] = \int \left\{ \frac{A}{2} \text{tr}(Q^2) - \frac{B}{3} \text{tr}(Q^3) + \frac{C}{4} [\text{tr}(Q^2)]^2 + \frac{L_1}{2} Q_{ij,k} Q_{ij,k} \right. \\ \left. + \frac{L_2}{2} Q_{ij,j} Q_{ik,k} + \frac{L_3}{2} Q_{ik,j} Q_{ij,k} + \frac{L_4}{2} Q_{kl} Q_{ij,k} Q_{ij,l} \right\} d\mathbf{r}, \quad (4)$$

where  $A$ ,  $B$ ,  $C$ , and  $L_i$  are system dependent parameters of a liquid crystal. The one-constant approximation,  $L_1 = L$  and  $L_2 = L_3 = L_4 = 0$ , is used here.

The one-constant approximation version of LdG theory can be written in reduced units. The radius of the colloidal particle  $R$  is used for reduction of all length related quantities, so that  $\mathbf{r}' = \mathbf{r}/R$ ,  $\nabla' = R\nabla$ , etc. Furthermore, we define

$$\tau = 27AC/8B^2, \quad \xi_R^2 = 27CL/8B^2R^2, \quad Q' = \sqrt{27C^2/8B^2}Q,$$

$$F' = (27^2 C^3 / 2B^4 R^3) F,$$

then the reduced free energy can be written,

$$F'[Q'(\mathbf{r}')] = \int \left\{ \frac{\tau}{2} \text{tr}(Q'^2) - \frac{\sqrt{6}}{4} \text{tr}(Q'^3) + \frac{1}{4} [\text{tr}(Q'^2)]^2 + \frac{\xi_R^2}{2} |\nabla' Q'|^2 \right\} d\mathbf{r}'.$$

After dropping all primes, with the implicit understanding that the reduced quantities are used, the free energy has the form in (1).

This convention, including the one-constant approximation and the use of  $R$  in the reduction of units, is often used in theoretical studies of related systems. One can see, for example, ref. 13, 25 and 27–29.

### B Parameters for the 5CB liquid crystal

5CB is a commonly used example of a real liquid-crystal system. At room temperature, the constants in the LdG model for 5CB were previously determined,  $A = -0.172 \times 10^6 \text{ J m}^{-3}$ ,  $B = -2.12 \times 10^6 \text{ J m}^{-3}$ ,  $C = 1.73 \times 10^6 \text{ J m}^{-3}$ , and  $L = 4 \times 10^{-11} \text{ J m}^{-1}$ .<sup>1,4–8,20,21</sup> This translates into

$$\tau = -0.2234 \quad (5)$$

and

$$\xi_R = 0.007209 \mu\text{m}/R \quad (6)$$

in 5CB.

### C Spectral approximation

The numerical calculation is carried out for the liquid-crystal structure inside a unit cell, which is defined by

$$\mathbf{R}_I = l_1 \mathbf{a}_1 + l_2 \mathbf{a}_2 + l_3 \mathbf{a}_3, \quad (7)$$

where a component of  $\mathbf{I}$ ,  $l_i$  ( $i = 1, 2, 3$ ), is an integer. The primitive vectors can be represented by Cartesian coordinates,  $\mathbf{a}_1 = (a_{11}, a_{12}, a_{13})$ ,  $\mathbf{a}_2 = (a_{21}, a_{22}, a_{23})$ , and  $\mathbf{a}_3 = (a_{31}, a_{32}, a_{33})$ . The corresponding reciprocal-lattice primitive vectors are  $\mathbf{b}_1 = (b_{11}, b_{12}, b_{13})$ ,  $\mathbf{b}_2 = (b_{21}, b_{22}, b_{23})$ , and  $\mathbf{b}_3 = (b_{31}, b_{32}, b_{33})$ , satisfying  $a_i \cdot \mathbf{b}_j = 2\pi\delta_{ij}$ . A reciprocal-lattice site is represented by the vector

$$\mathbf{G}_n = n_1 \mathbf{b}_1 + n_2 \mathbf{b}_2 + n_3 \mathbf{b}_3, \quad (8)$$

where a component of  $\mathbf{n}$ ,  $n_i$  ( $i = 1, 2, 3$ ), is an integer.

The reduced  $Q$  tensor is then represented by the Fourier series,

$$Q(\mathbf{r}) = \sum_{n_1=0}^{N_1-1} \sum_{n_2=0}^{N_2-1} \sum_{n_3=0}^{N_3-1} q_{n_1 n_2 n_3} \exp(i\mathbf{G}_n \cdot \mathbf{r}), \quad (9)$$

where  $N_i$  ( $i = 1, 2, 3$ ) is the truncation limit of the expanded series. The free energies of all structures present in Fig. 7 are computed by taking  $N_i = 64$ . Note that the periodic condition  $Q(\mathbf{r}) = Q(\mathbf{r} + \mathbf{R}_I)$  is naturally satisfied in this form. The coefficient of the expansion,  $q_n$ , is a  $3 \times 3$  tensor. Because of the original symmetry of the  $Q$  tensor, only 5 elements of  $q_n$  are independent. Inserting the expansion into the free energy expression, we obtain the free energy as a function of all these unknown elements. The free energy can then be minimized by using a standard

optimization method, such as L-BFGS,<sup>31</sup> which treats these unknown elements as minimizing variables. The optimal reciprocal-lattice primitive vectors  $\mathbf{b}_i$  are adjusted by a derivative-free optimization method such as the Mesh Adaptive Direct Search (MADS).<sup>33</sup> Their sizes and the relative angles between them are simultaneously adjusted. Some final values can be viewed in Table 1.

## D Boundary conditions

The direct incorporation of spherical surfaces of colloidal particles in the above three-dimensional expansion based on Cartesian coordinates is impossible. During the last decades, various numerical methods were proposed to deal with complex geometric domains. Examples are the fictitious domain method (also known as a domain embedding method)<sup>32</sup> and the diffuse domain method.<sup>46,47</sup> The basic idea here is to consider the entire domain inside a calculated cell, including the interior of the “hard” colloidal spheres.

Assume that the center coordinates of the  $k$ th particle are specified by  $\mathbf{r}_k$ . Associated with this particle, the coordinates of the spherical surface are represented by a variable  $\mathbf{r}$  satisfying  $|\mathbf{r} - \mathbf{r}_k| = 1$  in reduced units. In our application of the fictitious domain method, a few spherical surfaces in the calculated cell need to be considered. The numerical trick is to replace the surface energy (penalty term), eqn (2), which is designed for the spherical surface, by a new form that contains integration over the entire calculated cell,

$$F_s = \frac{w}{2} \int \phi(\mathbf{r}) |Q(\mathbf{r}) - Q_0(\mathbf{r})|^2 d\mathbf{r} - F_0. \quad (10)$$

The function

$$\phi(\mathbf{r}) = \begin{cases} 0, & \text{when } |\mathbf{r} - \mathbf{r}_k| > 1 \\ 1, & \text{when } |\mathbf{r} - \mathbf{r}_k| < 1, \end{cases} \quad (11)$$

truncates this term outside of all colloidal surfaces. The function  $Q_0(\mathbf{r})$ , which only needs to be specified inside the surfaces, is designed to follow an exact minimizer of  $F$  with the desired homeotropic anchoring boundary condition, which yields a constant  $F_0$ .

Consider the interior of a sphere of unit radius centered at the origin. For a radial hedgehog (RH) distribution,<sup>48,49</sup> the  $Q$  tensor is assumed to have the form

$$Q_{RH}(\mathbf{r}) = s(|\mathbf{r}|) \left( \frac{\mathbf{r}}{|\mathbf{r}|} \otimes \frac{\mathbf{r}}{|\mathbf{r}|} - \frac{1}{3} \mathbf{I} \right), \quad 0 < |\mathbf{r}| \leq 1, \quad (12)$$

with  $s(r)$  to be determined. In spherical coordinates, the minimization of  $F$  reduces to solving the Euler–Lagrange equation,

$$s''(r) + \frac{2}{r}s'(r) = 6s(r)/r^2 + \tau s - \frac{\sqrt{6}}{4}s^2 + \frac{2}{3}s^3 \quad (13)$$

with the boundary conditions  $s(0) = 0$ , and  $s(1) = 3S_0/2$ . The numerical solution of this well-specified differential equation can be obtained accurately before the full calculation of the current problem is conducted.

Having obtained  $Q_{RH}(\mathbf{r})$ , we simply let

$$Q_0(\mathbf{r}) = Q_{RH}(\mathbf{r} - \mathbf{r}_k) \quad (14)$$

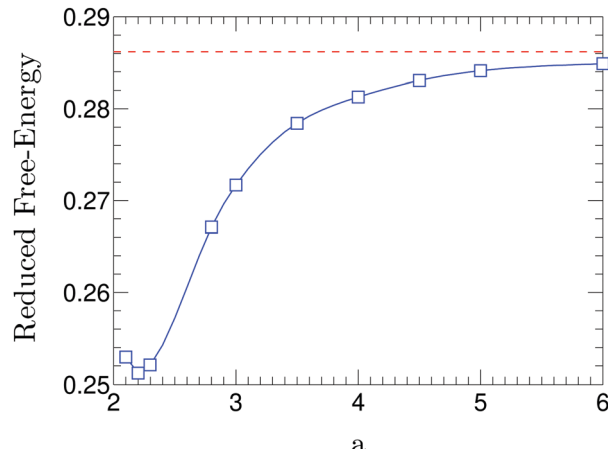


Fig. 9 A test of the current numerical approach. As the side length  $a$  of the unit cell is pushed to an asymptotically large number, the free energy converges to that of the Saturn ring solution (dashed line), obtained by a completely different numerical approach. A minimum of the system at  $a = 2.2$  can be seen. Squares represent the numerical solutions for a number of selected  $a$ .

when  $\mathbf{r}$  is within the unit radius of  $\mathbf{r}_k$ . When the sum of the free energy,  $F + F_s$ , is minimized over the entire cell by an implementation of the spectral method, all the interfaces between the colloids and the liquid crystal are enforced to follow the homeotropic boundary conditions when  $w$  is assumed large here.

To test this method, we benchmark the solutions of the free energy in an artificial case where a single spherical particle is placed at the center of a cubic unit cell, with periodic boundary conditions at the unit-cell surfaces, for  $\xi_R = 0.07071$ . Fig. 9 demonstrates two features. As  $a \rightarrow \infty$ , the free energy converges to the known Saturn-ring solution, given in the plot by the dashed line, as expected. A minimum around  $a = 2.2$  can be seen, which indicates that the new method can be used to locate a free energy minimum as a function of  $a$ , within the cubic constraint.

## Acknowledgements

We acknowledge the financial support from National Natural Science Foundation of China (Grant No. 11421101 and 11421110001), and an International Research Partnership Grant from the University of Waterloo that seeded this collaboration.

## References

- M. Ravnik and S. Žumer, *Liq. Cryst.*, 2009, **36**, 1201–1214.
- P. Poulin, H. Stark, T. C. Lubensky and D. A. Weitz, *Science*, 1997, **275**, 1770–1773.
- V. G. Nazarenko, A. B. Nych and B. I. Lev, *Phys. Rev. Lett.*, 2001, **87**, 075504.
- I. Mušević, M. Škarabot, U. Tkalec, M. Ravnik and S. Žumer, *Science*, 2006, **313**, 954–958.

- 5 M. Škarabot, M. Ravnik, S. Žumer, U. Tkalec, I. Poberaj, D. Babič, N. Osterman and I. Mušević, *Phys. Rev. E: Stat., Nonlinear, Soft Matter Phys.*, 2007, **76**, 051406.
- 6 U. Ognysta, A. Nych, V. Nazarenko, I. Mušević, M. Škarabot, M. Ravnik, S. Žumer, I. Poberaj and D. Babič, *Phys. Rev. Lett.*, 2008, **100**, 217803.
- 7 M. Ravnik, M. Škarabot, S. Žumer, U. Tkalec, I. Poberaj, D. Babič, N. Osterman and I. Mušević, *Phys. Rev. Lett.*, 2007, **99**, 247801.
- 8 M. Škarabot, M. Ravnik, S. Žumer, U. Tkalec, I. Poberaj, D. Babič, N. Osterman and I. Mušević, *Phys. Rev. E: Stat., Nonlinear, Soft Matter Phys.*, 2008, **77**, 031705.
- 9 M. Ravnik and S. Žumer, *Soft Matter*, 2009, **5**, 4520–4525.
- 10 U. M. Ognysta, A. B. Nych, V. A. Uzunova, V. M. Pergamenshchik, V. G. Nazarenko, M. S. Škarabot and I. Mušević, *Phys. Rev. E: Stat., Nonlinear, Soft Matter Phys.*, 2011, **83**, 041709.
- 11 U. Tkalec and I. Mušević, *Soft Matter*, 2013, **9**, 8140–8150.
- 12 A. Nych, U. Ognysta, M. Škarabot, M. Ravnik, S. Žumer and I. Mušević, *Nat. Commun.*, 2013, **4**, 1489.
- 13 Y. Wang, P. Zhang and J. Z. Y. Chen, *Phys. Rev. E*, 2017, **96**, 042702.
- 14 H. Stark, *Phys. Rep.*, 2001, **351**, 387–474.
- 15 S. Čopar, N. A. Clark, M. Ravnik and S. Žumer, *Soft Matter*, 2013, **9**, 8203–8209.
- 16 D. Kang, J. E. MacLennan, N. A. Clark, A. A. Zakhidov and R. H. Baughman, *Phys. Rev. Lett.*, 2001, **86**, 4052–4055.
- 17 T. Araki, M. Buscaglia, T. Bellini and H. Tanaka, *Nat. Mater.*, 2011, **10**, 303.
- 18 F. Serra, K. C. Vishnubhatla, M. Buscaglia, R. Cerbino, R. Osellame, G. Cerullo and T. Bellini, *Soft Matter*, 2011, **7**, 10945–10950.
- 19 T. Araki, F. Serra and H. Tanaka, *Soft Matter*, 2013, **9**, 8107–8120.
- 20 M. Ravnik and S. Žumer, *Soft Matter*, 2009, **5**, 269–274.
- 21 F. R. Hung, *Phys. Rev. E: Stat., Nonlinear, Soft Matter Phys.*, 2009, **79**, 021705.
- 22 J. Fukuda, M. Yoneyama and H. Yokoyama, *Phys. Rev. E: Stat., Nonlinear, Soft Matter Phys.*, 2002, **65**, 041709.
- 23 J. Fukuda, M. Yoneyama and H. Yokoyama, *Eur. Phys. J. E: Soft Matter Biol. Phys.*, 2004, **13**, 87–98.
- 24 O. Guzmán, E. B. Kim, S. Grollau, N. L. Abbott and J. J. de Pablo, *Phys. Rev. Lett.*, 2003, **91**, 235507.
- 25 J. Fukuda, H. Stark, M. Yoneyama and H. Yokoyama, *Phys. Rev. E: Stat., Nonlinear, Soft Matter Phys.*, 2004, **69**, 041706.
- 26 J. Fukuda, H. Yokoyama, M. Yoneyama and H. Stark, *Mol. Cryst. Liq. Cryst.*, 2005, **435**, 63–723.
- 27 J. Fukuda and H. Yokoyama, *Phys. Rev. Lett.*, 2005, **94**, 148301.
- 28 T. Kishita, K. Takahashi, M. Ichikawa, J. Fukuda and Y. Kimura, *Phys. Rev. E: Stat., Nonlinear, Soft Matter Phys.*, 2010, **81**, 010701.
- 29 T. Kishita, N. Kondo, K. Takahashi, M. Ichikawa, J. Fukuda and Y. Kimura, *Phys. Rev. E: Stat., Nonlinear, Soft Matter Phys.*, 2011, **84**, 19–22.
- 30 F. E. Mackay and C. Denniston, *Soft Matter*, 2014, **10**, 4430–4435.
- 31 S. Wright and J. Nocedal, *Numerical optimization*, Springer, 1999, vol. 35.
- 32 R. Glowinski, T.-W. Pan and J. Periaux, *Comput. Methods Appl. Mech. Eng.*, 1994, **111**, 283–303.
- 33 C. Audet and J. J. E. Dennis, *SIAM J. Optim.*, 2006, **17**, 188–217.
- 34 A. C. Callan-Jones, R. A. Pelcovits, V. A. Slavin, S. Zhang, D. H. Laidlaw and G. B. Loriott, *Phys. Rev. E: Stat., Nonlinear, Soft Matter Phys.*, 2006, **74**, 061701.
- 35 P. Poulin, V. Cabuil and D. A. Weitz, *Phys. Rev. Lett.*, 1997, **79**, 4862–4865.
- 36 S. B. Chernyshuk, O. M. Tovkach and B. I. Lev, *Phys. Rev. E: Stat., Nonlinear, Soft Matter Phys.*, 2014, **89**, 032505.
- 37 A. B. Nych, U. M. Ognysta, V. M. Pergamenshchik, B. I. Lev, V. G. Nazarenko, I. Mušević, M. S. Škarabot and O. D. Lavrentovich, *Phys. Rev. Lett.*, 2007, **98**, 057801.
- 38 M. Yada, J. Yamamoto and H. Yokoyama, *Phys. Rev. Lett.*, 2004, **92**, 185501.
- 39 U. Ognysta, A. Nych, V. Nazarenko, M. Skarabot and I. Musevic, *Langmuir*, 2009, **25**, 12092–12100.
- 40 Y. Tamura and Y. Kimura, *Appl. Phys. Lett.*, 2016, **108**, 011903.
- 41 Y. Tamura and Y. Kimura, *Soft Matter*, 2016, **12**, 6817–6826.
- 42 D. R. Nelson, *Nano Lett.*, 2002, **2**, 1125–1129.
- 43 M. Ravnik, G. P. Alexander, J. M. Yeomans and S. Žumer, *Proc. Natl. Acad. Sci. U. S. A.*, 2011, **108**, 5188–5192.
- 44 P. G. de Gennes and J. Prost, *The physics of liquid crystals*, Oxford university press, 1993.
- 45 N. J. Mottram and C. J. P. Newton, 2014, arXiv:1409.3542[cond-mat.soft].
- 46 J. Kockelkoren, H. Levine and W.-J. Rappel, *Phys. Rev. E: Stat., Nonlinear, Soft Matter Phys.*, 2003, **68**, 037702.
- 47 X. Li, J. Lowengrub, A. Rätz and A. Voigt, *Commun. Math. Sci.*, 2009, **7**, 81.
- 48 E. C. Gartland Jr and S. Mkaddem, *Phys. Rev. E: Stat. Phys., Plasmas, Fluids, Relat. Interdiscip. Top.*, 1999, **59**, 563.
- 49 A. Majumdar, *Eur. J. Appl. Math.*, 2012, **23**, 61–97.